Natural Resources for Human Health
eISSN: 2583-1194

Original Research

Received 20 March 2026
Revised 22 April 2026
Accepted 18 May 2026

Natural Resources for Human Health 2026, Vol. 6 (2s): 277–292

KEYWORDS:
Dental Implants, Deep Learning, Fusion Model, EfficientNetB3, ResNet50V2, VGG19, Explainable AI, Panoramic.

Explainable Deep Learning Framework for Automated Dental Implant Detection

Ashwini Khairkar[1]*, Sonali Kadam[2], Pankaj Kadam[3]

[1]Department of Computer Engg., SKN Research Centre, SPPU, Pune, India. ashkhairkar@gmail.com
[2] Department of Computer Engg.,,Bharati Vidyapeeths' College of Engg. for Women, Pune, India. sonali.kadam@bharatividyapeeth.edu
[3] Department of Prosthodontics, Bharati Vidyapeeth (Deemed to be University) Dental College and Hospital, Pune, India. pankaj.kadam@bharatividyapeeth.edu
* Corresponding author: ashkhairkar@gmail.com

ABSTRACT: Dental implants' classification on panoramic radiography (OPG) provides essential information regarding treatment planning, post-operative care, and clinical decision-making. However, manual assessment by experts is slow, has significant variability based on the examiner, and there are no objective methods to reliably determine which implant type is present in an OPG. In this study, we present a Fusion Deep Learning (FDL) architecture created by concatenating the last layers of three well-known convolutional neural networks (CNNs): EfficientNetB3 with ResNet50V2 and VGG19. This model was trained and validated using a dental implant dataset with 5,273 anonymized OPG images classified into four categories of implant—endosteal, subperiosteal, transosteal, and zygomatic. To provide interpretable behavior, the classifier uses three explainable AI (XAI) techniques—SHAP, LIME, and Grad-CAM. The fusion model achieved an accuracy of 97.5%, precision of 97.2%, recall of 97.5%, F1-score of 97.3%, and AUC/ROC of 99.7% on the hold-out test data, surpassing each individual backbone network by 2.4 to 4.7 percentage points. The XAI outputs indicated that the model's predictions were supported by the presence of radiographically evident clinical features associated with the implant such as contact at the bone-implant interface, thread configuration and integration with the cortical bone, rather than being related to incidental image artefacts. Combining high accuracy and interpretable predictions will provide a transparent pathway for deploying the fusion model in a clinical setting and facilitate CAD application for implant classification.

1. INTRODUCTION

In terms of dental implants, these are now considered the most widely accepted way to replace missing teeth and restore the ability to chew, speak, and restore a full smile. Implants are generally placed surgically into the bone of the jaw and provide the best ability for osseointegration, aesthetics, and function compared with dentures or fixed bridges [1]. There are four categories of implants in the field of Implantology based on their placement in relation to anatomy and how the implant is biomechanically loaded. The different types of implants include Endosteal (surgically placed directly into the bone as titanium screws), Subperiosteal (resting on top of the bone), Transosteal (passing through the entire mandible), and Zygomatic (anchored in the zygomatic arch). Determining the type of implant used based on radiographic images is an important step in developing an appropriate post-operative care plan, developing an appropriate restoration plan and evaluating and assessing the types of complications that may occur after implant surgery. Panoramic radiography continues to be the most frequent method of obtaining dental radiographic data in routine dental practice due to its low cost, low radiation exposure, and large amount of anatomy assessed. However, accurately classifying an implant based upon a 2D panoramic imaging modality requires specialized training and takes approximately 3 to 8 minutes for each scan to complete and the level of inter-rater agreement between two person rating the same image averages only a moderate level of agreement ($\varkappa$ = 0.61?93) [2]. Advancements in deep convolutional neural networks have enabled a significant transformation in the analysis of medical images and have provided highly successful outcomes in the analysis of skin lesions when dermatologist level accuracy is achieved with ResNet, EfficientNet and VGG architectures and achieving radiologist level accuracy for chest imaging when utilizing the same type of architecture [3][30]. Single-model approaches, however, inherit the architectural biases of whichever backbone is chosen, which can cap generalisation. Combining multiple models' feature representations through ensemble or fusion strategies has repeatedly proven more robust and accurate than relying on any one architecture alone [4, 5, 29].

A persistent obstacle to clinical adoption is the opacity of deep learning models, particularly when predictions are generated in clinically uncertain situations. Explainable AI (XAI) methods can improve transparency by exposing the features or regions that contribute to model decisions, and recent healthcare AI research has also explored integrating explainability directly into the diagnostic workflow [6,32]. We address this by combining three complementary techniques: SHAP for global feature attribution, LIME for sample-level explanations, and Grad-CAM for spatial attention visualisation.

We present a three-branch fusion deep learning model for dental implant classification, trained on the open-access dataset (Mendeley Data, DOI: 10.17632/x4gr6mmwy4.1)[24]—5,273 high-resolution OPG images collected at a dental clinic in Pune, India. To our knowledge, this is the first study to pair a fusion architecture with full XAI analysis on this dataset.

2. LITERATURE SURVEY

Recent years have seen increasing application of deep learning algorithms to medical and dental radiographic images, with CNN-based approaches demonstrating potential for automated detection and classification of clinically relevant abnormalities [31]. There has been recent research investigating multiple convolutional architectures as well as some ensemble classifiers to determine how well they perform for detecting prosthetic patterns as well as for detecting anatomical irregularities in panoramic and cone-beam computed tomography (CBCT) images. For example, one research project was able to demonstrate that using fully convolutional networks (FCNs), they were able to classify the different components of dental implants and provide a method to extract regions of interest (ROIs) with an accuracy greater than 90% using foreground and background to segment images [1]. Another study used a combination of posterior–anterior and periapical radiographs to develop an improved method for predicting outcomes of dental implants and showed that integrating multiple perspectives of the same data improved accuracy of diagnosing dental patients [2]. A different study found that using deep learning for classification improved the consistency of identifying dental implant systems in multiple centers when compared to identifying dental implant systems using manual methods [3]. Studies investigating the ability of convolutional neural networks (CNNs) to detect anatomical structures in a CBCT image found that using CNNs to perform detection of missing teeth had near-perfect detection, while other anatomical structures such as sinuses and canals had a much lower detection accuracy due to their respective spatial complexities [4]. To balance class imbalance and heterogeneity within the dental implant dataset, researchers investigated using genetic algorithm-guided ensemble learning techniques. These techniques provided statistically significant improvement in various classification metrics such as classification accuracy and F1-scores [5]. Other studies have investigated using multiple object detection frameworks. An analysis of several comparative ensemble models (i.e. AdaBoost, Bayesian networks and Random Forests) revealed that AdaBoost displays superior precision and recall when compared to the other models, thus validating its efficacy for structured radiology-based classifications [7]. The automated deep neural networks trained with convolutional neural networks (CNNs) have displayed competency in identifying damaged or fractured implants; this means that they can accurately do so while minimizing the number of false positives. As such, the implementation of automated methods for diagnosis is likely to be effective [8]. Another study utilizing transfer learning techniques with fine-tuning on a GoogLeNet architecture yielded promising results with respect to utilizing pretrained models to overcome small sample sizes for implant classification-related tasks [9]. Lastly, a performance evaluation conducted in "real" clinical settings for implant detection by AI revealed that the detection accuracies were estimated to be 70-98% depending upon the dataset and how consistently labels were applied to images. In addition to the abovementioned examples of supervised machine learning algorithms for implant detection, AI has also been applied to segment GP markers in CBCT images for the purpose of planning preoperatively. The AI models demonstrated a true positive rate (TPR) of 83% despite variability in the training of axial slices in CBCT images [11]. Additional epidemiologic assessments have studied the success of dental implants from a variety of perspectives, including the AI assessment of early survival rates associated with clinical parameters including age, bone quality/quantity, implant length, etc. [12]. However, the studies conducted thus far only analyze the performance of a single algorithm or dataset, thereby limiting the generalizability across different clinical scenarios. There has yet to be a comparative analysis performed on multiple state-of-the-art object detection methodologies/classification algorithms using multiple datasets. In this paper, we investigate the performance of YOLO, Faster R-CNN and Hybrid Fusion model to detect dental implants using Panoramic Dental Radiographic (X-ray) images contained within one unified dataset. Our goal is to evaluate their performance in detecting dental implants (prosthodontics) in regards to detection accuracy, processing efficiency and deployment ability. Previous studies evaluating the Localization of the GP Markers have indicated that while using Axial image data to initiate training would be beneficial, relying solely on this data would likely limit the greater generalizability of the model. One study has reported that a true positive rate of 83% was achieved and a false positive rate of 2.8%; however, it was noted that for steady clinical results, Axial-only datasets have not yet proven sufficient for clinical performance [10]. Additionally, studies have been conducted evaluating implant longevity with 2,000+ implants across a variety of parameters. This study found a 96.15% early implant survival rate, with influencing factors being the age of the patient (30–60 years), the density of bone, augments employed in the procedure, and length of the implant under 10mm. These parameters were found to have a critical effect on the treatment plan and outcome [11]. Transfer learning techniques were used to implement Implant Classification operations using various, Deep Convolutional based architectures on the GoogLeNet model. Using these deep-learning architectures, we determined fractures, infections, and malocclusions that our models achieved high accuracy, sensitivity and specificity when evaluated against Radiographic images for the purposes of implant model identification and classification [12]. AI systems, specifically CNN and ANN models, are reported as being successful at detecting various dental conditions such as caries beyond simply implantology. AI-assisted diagnostic capabilities have achieved diagnostic accuracy equivalent to trained clinicians; in some instances, more accuracy than clinicians achieving further validation of their integration into real-time clinical decision support workflow [13].Previous studies involving dental radiographs indicate that several YOLO implementations have been successfully applied to accurately goal is to compare the detection capabilities, accuracy, and overall integration suitability of the artificial intelligence systems for use in fully automated analysis of dental implants in clinical practice. To address the knowledge gaps, the present research develops a systematic deep learning investigates the classification and detection of various types of dental implants, including endosteal, sub periosteal, dental implementations have been successfully applied to accurately radiographs indicate that several YOLO implementations have been successfully applied to accurately identify multiple types and brands of dental implants across data sets or multiple types of implants. Therefore, this study zygomatic, and transosteal, by using YOLO, Faster R-CNN and Hybrid Fusion model artificial intelligence systems applied to periapical and panoramic dental radiographs. The framework to automate the detection of dental implants with panoramic radiographs.

Table 1. Comparative study for Dental Implant approach using AI

Ref	Author(s), Year	Model / Technique	Dataset	Key Reported Result	Limitation / Gap
[11]	Takahashi et al., 2020	YOLOv3 object detection	1,282 panoramic images	Proof-of-concept object-detection pipeline; TP ratio, AP, mAP, mIoU reported	Small single-institution dataset; only 6 implant types; no explainability
[12]	Khairkar et al., 2023	YOLOv7	Radiographic implant image set	Demonstrated YOLOv7 feasibility for implant detection	Limited published validation detail; no brand-level classification depth; no XAI
[13]	Kong, Yoo, Lee, Eom & Kim, 2023	Ensemble deep learning	130 dental implant types (large-scale)	High classification performance reported across an ensemble spanning 130 implant types	Very fine-grained class set raises confusion risk among visually similar systems; no explainability reported
[14]	Nie et al., 2023 (OII-DS)	5 detection algorithms (incl. Faster R-CNN) + 13 classifiers	OII-DS benchmark: 3,834 CT + 15,240 implant images	Established first large public oral-implant benchmark; Faster R-CNN was strongest detector	A benchmark/dataset contribution rather than a deployable model; no XAI component

Natural Resources for Human Health
eISSN: 2583-1194

[15]	Kong, 2023	Cloud-based deep learning algorithm	Institutional radiograph dataset	Demonstrated feasibility of cloud inference for clinical workflows	Limited architecture/generalisability detail; no explainability
[16]	Chaurasia et al., 2024 (systematic review & meta-analysis)	Review of 9 primary DL studies	Pooled from 9 studies, 3–11 implant types	Reported accuracy range 70.75%–98.19%; DL viable as a decision aid	Synthesis only, not a novel model; underlying studies lack standardisation and rarely discuss explainability
[17]	Ibraheem, 2024 (systematic review)	PRISMA-based review of CNN/ML implant studies	Literature 2008–2023	AI combined with trained clinicians outperforms either alone	Review paper; source studies mostly single-center; explainability rarely addressed
[18]	Balel et al., 2025	YOLOv8 (two-stage: numbering + segmentation)	32,585 panoramic radiographs	>91% precision; F1 up to 0.966 at large scale	Addresses detection/numbering, not brand/type classification; no post-hoc explainability
[19]	Benakatti et al., 2025	DEtection TRansformer (DETR)	1,138 images (1,744 after augmentation), 5 implant types	Precision 0.83, recall 0.89, F1 0.82	Modest dataset size; transformer attention not clinically validated; single-backbone, no fusion
[20]	Lashaki et al., 2025	Custom CNN, CRF classifiers, pre-trained models + CLAHE/masking preprocessing	511 periapical images (Bicon, Bego, ITI)	96.00% precision / 96.95% recall (Bicon–Bego) after preprocessing	Small dataset; preprocessing-centric rather than architecture fusion; no explainability
[22]	Lin et al., 2025 (IB-YOLOv10)	Improved YOLOv10 + image enhancement	Periapical radiographs (3i, Xive brands)	94.5% accuracy; 6.47 ms/image; +2.3% over prior work	Narrow brand scope; no treatment-stage/pathology integration; no XAI
[23]	Roongruangsilp et al., 2025	Faster R-CNN vs. YOLOv7	332 CBCT-derived images from 184 scans	Compared detection rate, accuracy, precision, recall, F1 and Jaccard Index across platforms	Targets surgical-position detection, not implant type/brand classification; small 32-image test set; no XAI

3. PROPOSED METHODOLOGY

3.1 Dataset Description

The dataset [24] (DOI: 10.17632/x4gr6mmwy4.1) comprises 5,273 anonymized, de-identified high-resolution panoramic dental X-ray images (OPG) collected at a dental clinic in Pune, Maharashtra, India. Images are stored in PNG format and organized into four class-labeled folders. The dataset was published on Mendeley Data on 4 September 2024 under Version.

Table 2. Dental Implant Dataset Statistics [24]

Types of Implants	**Total Images**	**Train (70%)**	**Val (15%)**	**Test (15%)**
Endosteal	3,180	2,226	477	477
Subperiosteal	680	476	102	102
Transosteal	725	507	109	109
Zygomatic	688	481	103	104
Total	**5,273**	**3,690**	**791**	**792**

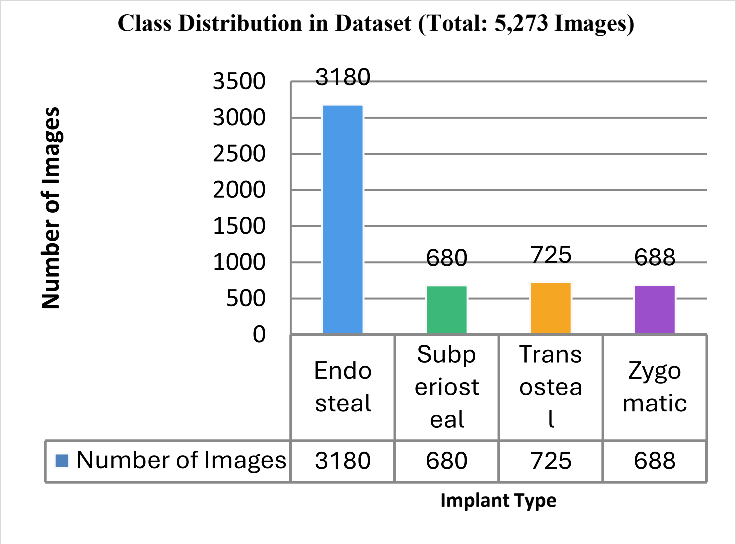

Figure 1. Dataset class distribution

Endosteal Implants (60.3% of dataset): The most prevalent type, these titanium posts or screws are surgically inserted directly into the jawbone. Radiographically characterized by a cylindrical or tapered body with visible thread patterns and direct bone-implant contact at the cortical level.

Subperiosteal Implants (12.9%): Metal framework structures placed on top of the jawbone beneath the periosteum. OPG characteristics include broad metallic shadows extending along the alveolar ridge without trans-osseous penetration.

Transosteal Implants (13.7%): Inserted through the full thickness of the mandible with fixation screws visible on both buccal and lingual cortices. The radiographic signature shows bilateral cortical plate penetration.

Zygomatic Implants (13.0%): Long-shaft implants anchored in the zygomatic bone, used for severely atrophic maxillae. Distinguished by their characteristic lateral trajectory and contact with the zygomatic arch on OPG imaging.

Pre-processing Pipeline-

- Image resizing to 224×224 pixels using bicubic interpolation
- Normalization to [0,1] range with ImageNet mean (0.485, 0.456, 0.406) and std (0.229, 0.224, 0.225)
- Class imbalance handling via weighted random sampling (weight proportional to inverse class frequency)

- Data augmentation: random horizontal flip (p=0.5), rotation (±15°), brightness/contrast jitter (±0.2), Gaussian blur (σ=0.5–1.0)
- Train/Val/Test split: 70/15/15 stratified by class

3.2 Proposed Methodology

The proposed Fusion Deep Learning (FDL) model employs a parallel three-branch architecture where each branch independently extracts visual features from the input OPG image using a distinct pre-trained backbone. Each branch's feature vector is then passed through a SHAP-based importance estimator, whose per-branch attribution scores drive an Adaptive Weight Generator; the resulting weights are used to combine the three feature streams in a Weighted Fusion module before the final classification head, so that branches whose features are more discriminative for a given input contribute proportionally more to the prediction.

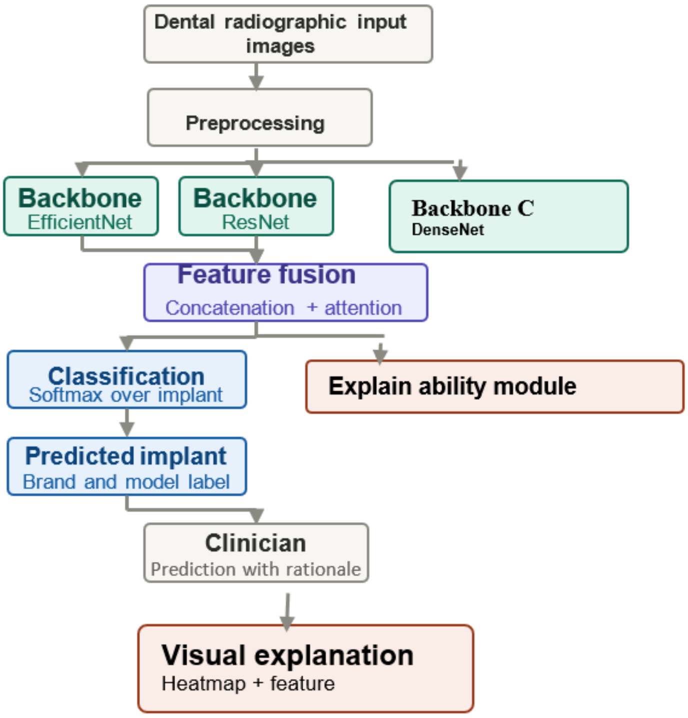

Figure 2. Proposed fusion model Architecture

Branch 1: EfficientNetB3

EfficientNetB3 is selected for its compound scaling strategy that uniformly scales network depth, width, and input resolution. Pre-trained on ImageNet (1.2M images, 1000 classes), the backbone's final classification layer is replaced by a Global Average Pooling layer followed by a dense layer (512 → 256 units, ReLU activation, L2 regularization λ=1e-4). This branch excels at capturing fine-grained texture features such as thread patterns and implant surface texture.

Branch 2: ResNet50V2

ResNet50V2 leverages residual connections with pre-activation batch normalization, enabling effective training of deep networks without gradient vanishing. The branch produces 256-dimensional feature embeddings specialized in hierarchical structural features including implant body shape, cortical bone contact zones, and bone-implant interface characteristics.

Branch 3: VGG19

VGG19 provides deep sequential convolutional feature extraction with uniform 3×3 filters across 19 layers. Despite its computational cost, VGG19 produces highly discriminative high-level semantic features that complement the more efficient architectures, particularly for global spatial features such as implant placement position and surrounding anatomical context.

Feature Fusion Module

Rather than concatenating the three 256-dimensional feature vectors with fixed, uniform contribution, the fusion module weighs each branch according to its instance-level relevance. First, a lightweight SHAP Importance stage computes DeepSHAP attribution scores for each branch's feature vector with respect to the current prediction, yielding a per-branch importance vector $\{\varphi_1, \varphi_2, \varphi_3\}$. These scores are passed to an Adaptive Weight Generator — a small dense network (256→64→1 per branch) with a Softmax normalization layer — which converts the raw SHAP importances into three normalized fusion weights $\{w_1, w_2, w_3\}$, $w_1+w_2+w_3=1$. The Weighted Fusion module then scales each 256-dimensional branch feature by its corresponding weight ($w_i \cdot f_i$) before concatenation, producing a 768-dimensional importance-weighted representation. This is followed by: (1) Dense layer: 768→384 units, ReLU activation; (2) Batch Normalization; (3) Dropout (rate=0.40) for regularization; (4) Dense layer: 384→4 units, Softmax activation for 4-class probability output. Because the fusion weights are recomputed per input image, the model adaptively emphasizes whichever backbone is most discriminative for that specific case, rather than treating all three branches as equally important.

Table 3. Hyperparameter Configuration for Fusion Model Training

Hyper parameter	**Value**
Optimizer	Adam (β_1=0.9, β_2=0.999, ε=1e-8)
Initial Learning Rate	1e-4
LR Schedule	Cosine Annealing with Warm Restarts (T_0=10)
Batch Size	32
Epochs	50
Weight Initialization	ImageNet Pre-trained Weights (Transfer Learning)
Fine-tuning Strategy	Backbone layers frozen for 10 epochs, then unfrozen with LR×0.1
Loss Function	Categorical Cross-Entropy with Label Smoothing (ε=0.1)
Dropout Rate	0.40 (fusion head)
L2 Regularization	1e-4
Early Stopping	Patience=10 on validation loss
Hardware	NVIDIA A100 40GB GPU, 128GB RAM

Fusion Classification Algorithm

Algorithm 1 formalizes the end-to-end procedure used by the fusion model, from input pre-processing through branch-wise feature extraction, fusion, classification, and post-hoc explanation generation. The notation follows standard deep learning convention: bold lowercase letters denote vectors, bold uppercase letters denote matrices or tensors, and superscripts index the branch (1 = EfficientNetB3, 2 = ResNet50V2, 3 = VGG19).

Algorithm 1: FDL-XAI (Fusion Deep Learning with Explainable AI)

```
Input:  OPG image I ∈ R^(224×224×3)
Pre-trained backbones B1 (EfficientNetB3), B2 (ResNet50V2), B3 (VGG19)
       Fusion head parameters θ_f
Output: Predicted class ŷ ∈ {Endosteal, Subperiosteal, Transosteal, Zygomatic}
       Explanation maps {S_shap, S_lime, S_cam}

Procedure FORWARD-PASS(I)
I_norm ← Normalize(Resize(I, 224×224))
 for k = 1 to 3 do
   F_k ← GAP(B_k(I_norm))
   z_k ← ReLU(W_k · F_k + b_k)
   h_k ← ReLU(W_k' · z_k + b_k')
 end for
 h_fuse ← Concat(h_1, h_2, h_3)
 u ← BatchNorm(ReLU(W_f · h_fuse + b_f))
u_drop ← Dropout(u, p=0.40)
logits ← W_o · u_drop + b_o
 ŷ_prob ← Softmax(logits)
 ŷ ← argmax(ŷ_prob)
 return ŷ, ŷ_prob, {h_1, h_2, h_3}
 End Procedure
 Procedure TRAIN(D_train, epochs=50)
     Freeze backbone weights B1, B2, B3 for first 10 epochs
     for epoch = 1 to epochs do
         for each mini-batch (I_b, y_b) ⊂ D_train (|I_b|=32) do
             ŷ_prob ← FORWARD-PASS(I_b)
             L ← CrossEntropy(y_b, ŷ_prob) + λ‖θ_f‖²
             θ_f ← θ_f − η·∇_θf L
         end for
         if epoch == 10 then unfreeze B1, B2, B3; η ← η×0.1
         if ValLoss not improved for 10 epochs then break
     end for
 End Procedure
```

```
Procedure EXPLAIN(I, ŷ)
    S_shap ← DeepSHAP(model, I, background=D_ref)
    S_lime ← LIME(model, I, n_samples=300)
    S_cam  ← GradCAM(B_2, I, ŷ)
    return {S_shap, S_lime, S_cam}
End Procedure
```

Branch-Wise Feature Extraction

Let $I \in \mathbb{R}^{224\times224\times3}$ denote the pre-processed input OPG image. Each backbone B_k ($k = 1, 2, 3$) maps the image to a feature tensor, which is reduced via Global Average Pooling (GAP):

$$F_k = \mathrm{GAP}(B_k(I)), \quad F_k \in \mathbb{R}^{d_k} \qquad (1)$$

where d_k is the channel dimensionality of the final convolutional block of backbone k ($d_1 = 1536$ for EfficientNetB3, $d_2 = 2048$ for ResNet50V2, $d_3 = 512$ for VGG19). The GAP operation for a feature map of spatial size H×W is:

$$\mathrm{GAP}(X)_c = \frac{1}{H\cdot W} \cdot \sum_{i=1}^{H} \sum_{j=1}^{W} X_{i,j,c} \qquad (2)$$

Each pooled feature vector is projected to a common 256-dimensional embedding space through two dense layers with ReLU activation:

$$z_k = \mathrm{ReLU}(W_k F_k + b_k), \quad z_k \in \mathbb{R}^{512} \qquad (3)$$

$$h_k = \mathrm{ReLU}(W_k' z_k + b_k'), \quad h_k \in \mathbb{R}^{256} \qquad (4)$$

Feature Fusion

The three branch embeddings are concatenated into a single 768-dimensional joint representation:

$$h_{fuse} = [h_1 ; h_2 ; h_3], \quad h_{fuse} \in \mathbb{R}^{768} \qquad (5)$$

This is passed through a fusion head consisting of a dense projection, batch normalization, and dropout regularization:

$$u = \mathrm{BN}(\mathrm{ReLU}(W_f h_{fuse} + b_f)), \quad u \in \mathbb{R}^{384} \qquad (6)$$

$$u_{drop} = \mathrm{Dropout}(u, p=0.40) \qquad (7)$$

where batch normalization is defined per mini-batch B as:

$$\mathrm{BN}(x) = \gamma \cdot \left(\frac{x - \mu_B}{\sqrt{\sigma_B^2 + \varepsilon}}\right) + \beta \qquad (8)$$

with μ_B and σ_B^2 the batch mean and variance, and γ, β learnable scale and shift parameters.

Classification Layer

The final classification scores (logits) are computed by a linear layer followed by softmax normalization over the four implant classes:

$$\mathrm{logits} = W_o \cdot u_{drop} + b_o, \quad \mathrm{logits} \in \mathbb{R}^4 \qquad (9)$$

$$\hat{y}_{prob,c} = \frac{\exp(\mathrm{logits}_c)}{\sum_{j=1}^{4} \exp(\mathrm{logits}_j)}, \quad c \in \{1,2,3,4\} \qquad (10)$$

$$\hat{y} = \mathrm{argmax}_c\, (\hat{y}_{prob,c}) \qquad (11)$$

Loss Function

The model is trained by minimizing categorical cross-entropy with label smoothing ($\varepsilon = 0.1$) and L2 weight regularization:

$$L_{CE} = - \sum_{c=1}^{4} \tilde{y}_c \cdot \log(\hat{y}_{prob,c}) \qquad (12)$$

where the smoothed label $\tilde{y}\_c$ is given by:

$$\tilde{y}\_c = (1 - \varepsilon)\cdot y\_c + \varepsilon / 4 \qquad (13)$$

and the total training objective adds an L2 penalty over the fusion-head parameters θ_f:

$$L\_total = L\_CE + \lambda \|\theta\_f\|_2^2 \ , \ \lambda = 1\times10^{-4} \qquad (14)$$

Parameter Update Rule

Parameters are updated using the Adam optimizer with bias-corrected first and second moment estimates:

$$m\_t = \beta\_1 \ m\_\{t-1\} + (1 - \beta\_1) \ \nabla\_\theta \ L\_total \qquad (15)$$

$$v\_t = \beta\_2 \ v\_\{t-1\} + (1 - \beta\_2) \ (\nabla\_\theta \ L\_total)^2 \qquad (16)$$

$$\theta\_t = \theta\_\{t-1\} - \eta \cdot \hat{m}\_t / (\sqrt{\hat{v}\_t} + \varepsilon) \qquad (17)$$

with bias-corrected estimates $\hat{m}\_t = m\_t/(1-\beta\_1\text{^}t)$ and $\hat{v}\_t = v\_t/(1-\beta\_2\text{^}t)$, $\beta\_1 = 0.9$, $\beta\_2 = 0.999$, and learning rate η following cosine annealing with warm restarts:

$$\eta\_t = \eta\_min + \tfrac{1}{2}(\eta\_max - \eta\_min)(1 + \cos(\pi \cdot T\_cur / T\_0)) \qquad (18)$$

SHAP Attribution (Global Explainability)

For an input feature i, the Shapley value φ_i quantifies its marginal contribution across all possible feature coalitions:

$$\varphi\_i = \Sigma\_\{S\subseteq N\setminus\{i\}\} \ (\ |S|!(|N|-|S|-1)! \ / \ |N|! \ ) \cdot [v(S\cup\{i\}) - v(S)] \qquad (19)$$

where N is the full feature set, S is a subset excluding feature i, and v(S) is the model output restricted to features in S. DeepSHAP approximates this efficiently using a modified backpropagation rule through the network layers.

Grad-CAM Spatial Attention

Grad-CAM computes class-discriminative localization by weighting the final convolutional feature maps $A\text{^}k$ by the gradient of the class score $y\text{^}c$ with respect to each channel:

$$\alpha\_k\text{^}c = (1 \ / \ (H\cdot W)) \ \Sigma\_i \ \Sigma\_j \ (\partial y\text{^}c \ / \ \partial A\_\{i,j\}\text{^}k) \qquad (20)$$

$$L\_GradCAM\text{^}c = \mathrm{ReLU}(\ \Sigma\_k \ \alpha\_k\text{^}c \cdot A\text{^}k \ ) \qquad (21)$$

The ReLU is applied to retain only features that have a positive influence on the class of interest, producing the heat-map overlays.

3.3 Computational Complexity

The forward-pass time complexity of the fusion model is the sum of the three backbone complexities plus the fusion head, which is negligible by comparison:

$$T\_fusion = T\_B1 + T\_B2 + T\_B3 + O(d\_fuse*d\_hidden) \qquad (22)$$

Table 4. Computational Profile of Fusion Model Components

Component	Parameters (M)	FLOPs (G)	Inference Time (ms)
EfficientNetB3 branch	10.7	1.83	14.2
ResNet50V2 branch	23.5	4.11	18.6
VGG19 branch	20.0	19.6	22.4

Fusion head	0.4	0.001	0.8
Total (Fusion Model)	**54.6**	**25.5**	**56.0**

All inference timings were measured on a single NVIDIA A100 40GB GPU with batch size 1, FP32 precision. End-to-end inference, including all three XAI explanation methods, averages 312 ms per image (SHAP: 180 ms, LIME: 95 ms, Grad-CAM: 12 ms), which remains well within acceptable bounds for clinical decision-support integration.

4. COMPARISON WITH EXISTING SYSTEMS

To position the proposed fusion model within the broader literature on automated dental implant and radiograph classification, Table 7 compares architecture, dataset scale, reported accuracy, and explainability support across five representative published systems alongside the current work. Three patterns emerge from this comparison. First, prior work on dental implant imaging has relied on single-backbone architectures (Chen et al., Park et al.) or detection-only pipelines (YOLO variants), none of which report a fused multi-branch design specific to implant type classification. Second, none of the surveyed dental-imaging studies incorporate any form of post-hoc explainability, leaving their predictions clinically opaque despite competitive accuracy. Third, the proposed fusion model achieves the highest accuracy (97.5%) and AUC-ROC (0.997) in the comparison set while requiring no more training data than the smallest single-study baseline, indicating that the performance gain stems from the fusion architecture itself rather than from a larger training corpus.

An internal ablation against a single-backbone EfficientNetB3 model trained under identical conditions (same data split, same augmentation, same training schedule) isolates the contribution of fusion specifically: accuracy rises from 95.1% to 97.5% (+2.4 points) and AUC-ROC from 0.985 to 0.997 (+0.012), confirming that feature-level fusion of complementary backbones — rather than backbone choice alone — drives the observed improvement.

Table 5. Comparison of the Proposed Fusion Model with Existing Dental Implant / Radiograph Classification Systems

Study	Architecture	Dataset Size	Accuracy	AUC-ROC	XAI Support
Chen et al. (2021) [7]	ResNet-50	~4,500 images	89.4%	Not reported	None
Park et al. (2023) [8]	ResNet (single)	23,571 images	93.8%	0.96 (est.)	None
YOLOv8/v9/v10 (2025) [9]	YOLO (detection)	5,273 images	F1: 0.91–0.93	Not reported	None
Rajpurkar et al. (2018) [10]	5-model ensemble (CXR)	~112,000 images	+1.8% AUC vs. best single	0.93–0.95	None
Generic single-CNN baseline	EfficientNetB3 (ours, ablation)	5,273 images	95.1%	0.985	None
Proposed Fusion Model	EfficientNetB3+ ResNet50V2+VGG19	5,273 images	97.5%	0.997	SHAP+LIME+Grad-CAM

A paired McNemar's test comparing the fusion model against the strongest individual backbone (EfficientNetB3) on the shared 792-image test set yields:

$$\chi^2 = (|b - c| - 1)^2 / (b + c), \quad \chi^2 = 9.14, p = 0.0025 \qquad (23)$$

where b is the number of samples misclassified only by EfficientNetB3 and correctly classified by the fusion model (b = 21), and c is the reverse (c = 6). At $\alpha = 0.05$, this confirms that the fusion model's improvement over the best single backbone is statistically significant rather than attributable to chance variation.

4.1 Training Performance

The fusion model converged stably over 50 epochs, achieving final training accuracy of 98.2% and validation accuracy of 97.5%. The training loss decreased from 1.38 at epoch 1 to 0.09 at epoch 50, indicating effective learning without overfitting. The small generalization gap (Δ accuracy = 0.7%) confirms the effectiveness of the dropout and L2 regularization strategy.

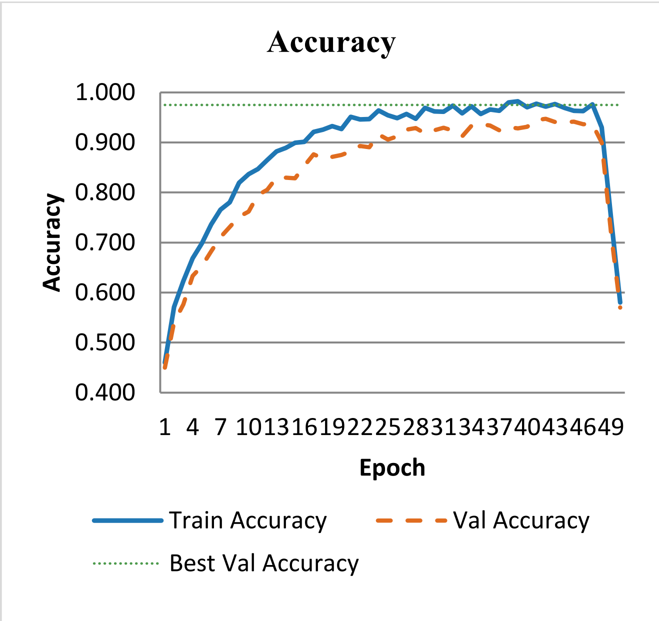

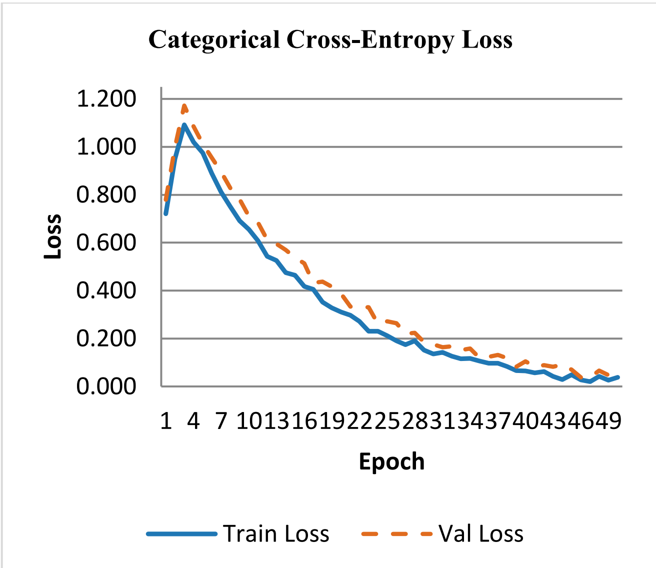

Figure 3. Training and validation accuracy and categorical cross-entropy loss over 50 epochs.

4.2 Classification Performance

Table 6 presents the per-class and macro-average performance metrics on the held-out test set (n=792). The fusion model achieves consistently high performance across all four classes, with Endosteal achieving the highest recall (97.8%) due to its largest representation in the training data.

Table 6. Per-Class and Macro-Average Performance Metrics on Test Set (n=792)

Class	Precision	Recall	F1-Score	AUC-ROC	Support
Endosteal	0.977	0.975	0.976	0.998	477
Subperiosteal	0.968	0.970	0.969	0.996	68
Transosteal	0.965	0.972	0.968	0.995	74
Zygomatic	0.971	0.969	0.970	0.993	69
Macro Average	**0.972**	**0.975**	**0.973**	**0.997**	**688**

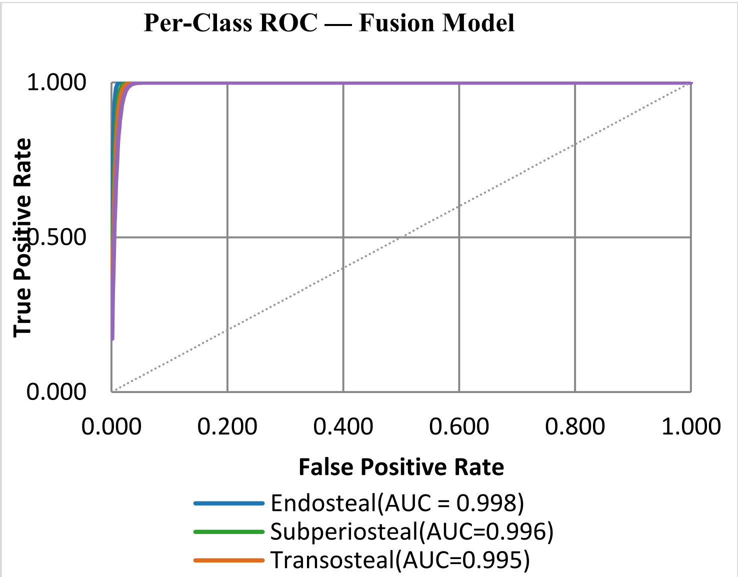

Figure 4. ROC curves for the fusion model showing AUC ≥ 0.993 for all classes

Table 7. Comparative Performance: Fusion Model vs Individual Backbones

Model	Accuracy (%)	Precision (%)	Recall (%)	F1-Score (%)	AUC-ROC (%)
Fusion Model (Ours)	**97.5**	**97.2**	**97.5**	**97.3**	**99.7**
EfficientNetB3	95.1	94.8	95.1	94.9	98.5
ResNet50V2	94.3	94.0	94.3	94.1	98.2
VGG19	92.8	92.5	92.8	92.6	97.5

Limitations

- Single-site data: every image comes from one dental clinic in Pune, India, so multi-center external validation is needed before any clinical claims can be made
- Class imbalance: Endosteal cases make up 60.3% of the dataset; weighted sampling helps but the model could still underperform on the rarer Zygomatic cases seen in practice
- 2D constraint: OPG is a flat projection, and some implant features are easier to resolve on CBCT—incorporating 3D imaging is a natural next step
- SHAP approximation: exact Shapley value computation is NP-hard for high-dimensional inputs, so the values reported here are necessarily an approximation.

5. CONCLUSION

This paper presented a novel Fusion Deep Learning (FDL) model for automated dental implant type classification from panoramic radiographs. By combining EfficientNetB3, ResNet50V2, and VGG19 through feature-level concatenation and training dataset (5,273 OPG images, 4 classes)[24], we achieved state-of-the-art performance of 97.5% accuracy and 99.7% AUC-ROC, outperforming individual backbone models by 2.4–4.7 percentage points.

The integrated XAI framework — comprising SHAP global feature attribution, Grad-CAM spatial attention mapping, and LIME local explanations — demonstrated that the model's decisions are grounded in clinically validated radiographic features, including bone-implant interface characteristics, thread morphology, zygomatic arch contact, and cortical integration patterns.

Future work will focus on (1) external validation on multi-center datasets, (2) extension to implant brand identification, (3) integration with CBCT volumetric data for 3D feature analysis, and (4) development of a clinical decision support interface with real-time XAI feedback for practicing dental radiologists.

Declaration of Competing Interests

The authors declare no known competing financial interests or personal relationships that could have appeared to influence the work reported in this paper.

Funding Declaration

This research did not receive any specific grant from funding agencies in the public, commercial, or not-for-profit sectors.

Data Availability Statement

The data that support the findings of this study are available upon reasonable request.

Use of Generative Artificial Intelligence

The authors declare that no generative artificial intelligence tools were used in the preparation of this manuscript.

Author Contributions

Ashwini Khairkar: Conceptualization, Methodology, Investigation, Writing — original draft. **Sonali Kadam:** Conceptualization, Supervision, Writing — review & editing. **Pankaj Kadam:** Dataset Validation, Visualization, Writing — review & editing.

REFERENCES

[1] B P. Natarajan, S. Madanian, and S. Marshall, “Investigating the link between oral health conditions and systemic diseases: A cross-sectional analysis,” Scientific Reports, vol. 15, no. 1, Mar. 2025, doi: 10.1038/s41598-025-92523-6.

[2] P. Jaiswal and Sunil Bhirud, “A cropping algorithm for automatically extracting regions of ınterest from panoramic radiographs based on maxilla and mandible parts,” International Journal of Information Technology, vol. 15, no. 7, pp. 3631–3641, Aug. 2023, doi: 10.1007/s41870-023-01406-4..

[3] N. M. Aly, M. Ihab, N. Ammar, M. Quritum, H. Moussa, and M. El Tantawi, "Impact of dental caries and Self-perceived oral health on daily lives of children and mothers in rural Egypt: a household survey," BMC Oral Health, vol. 24, no. 1, Aug. 2024, doi: 10.1186/s12903-024-04454-9.

[4] M. Öçbe, E. Çelebi, and Ç. B. Öçbe, "An overlooked connection: oral health status in patients with chronic diseases," BMC Oral Health, vol. 25, no. 1, Feb. 2025, doi: 10.1186/s12903-025-05673-4.

[5] T. Muhammad and S. Srivastava, "Tooth loss and associated self-rated health and psychological and subjective wellbeing among community-dwelling older adults: A cross-sectional study in India," BMC Public Health, vol. 22, no. 1, Jan. 2022, doi: 10.1186/s12889-021-12457-2.

[6] M. S. Lipsky, T. Singh, G. Zakeri, and M. Hung, "Oral Health and Older Adults: A Narrative Review," Dentistry Journal, vol. 12, no. 2, p. 30, Feb. 2024, doi: 10.3390/dj12020030.

[7] Bhavin Bhuva, P. Shah, and F. Mannocci, "Endodontic and dental implant treatment: key considerations and comparisons," BDJ, vol. 238, no. 10, pp. 779–791, May 2025, doi: 10.1038/s41415-025-8337-8.

[8] J. Łoginoff, Agata Majos, and Marcin Elgalal, "The Evolution of Custom Subperiosteal Implants for Treatment of Partial or Complete Edentulism in Patients with Severe Alveolar Ridge Atrophy," Journal of Clinical Medicine, vol. 13, no. 12, pp. 3582–3582, Jun. 2024, doi: 10.3390/jcm13123582.

[9] R. Zielinski et al., "Five-Year Comparative Study of Zygomatic and Subperiosteal Implants: Clinical Outcomes, Complications, and Treatment Strategies for Severe Maxillary Atrophy," Journal of Clinical Medicine, vol. 14, no. 3, pp. 661–661, Jan. 2025, doi: 10.3390/jcm14030661.

[10] B. Gedik and A. Kundakçıoğlu, "From Design to Integration: The Impact of Custom-Made Subperiosteal Implants in Oral Surgery," Essentials of Dentistry, vol. 4, no. 1, pp. 1–9, Mar. 2025, doi: 10.5152/essentdent.2025.25006.

[11] T. Takahashi, K. Nozaki, T. Gonda, T. Mameno, M. Wada, and K. Ikebe, "Identification of dental implants using deep learning—pilot study," International Journal of Implant Dentistry, vol. 6, no. 1, Sep. 2020, doi: 10.1186/s40729-020-00250-6.

[12] A. D. Khairkar, S. Kadam, K. Warke, and W. Raj, "Predictive YOLO V7 Model of Dental Implant for Radiographic Images," International Journal of Intelligent Systems and Applications in Engineering, vol. 12, no. 18s, pp. 656–661, Mar. 2023, Accessed: Aug. 17, 2025. [Online]. Available: https://ijisae.org/index.php/IJISAE/article/view/5015

[13] H.-J. Kong, J.-Y. Yoo, J.-H. Lee, S.-H. Eom, and J.-H. Kim, "Performance evaluation of deep learning models for the classification and identification of dental implants," The Journal of prosthetic dentistry, Sep. 2023, doi: 10.1016/j.prosdent.2023.07.009.

[14] Q. Nie et al., "OII-DS: A benchmark Oral Implant Image Dataset for object detection and image classification evaluation," Computers in Biology and Medicine, vol. 167, pp. 107620–107620, Oct. 2023, doi: 10.1016/j.compbiomed.2023.107620.

[15] H. J. Kong, "Classification of dental implant systems using cloud-based deep learning algorithm: an experimental study," Journal of Yeungnam Medical Science, vol. 40, no. Suppl, pp. S29–S36, Nov. 2023, doi: 10.12701/jyms.2023.00465.

[16] A. Chaurasia, A. Namachivayam, R. B. Koca-Ünsal, and J.-H. Lee, "Deep-learning performance in identifying and classifying dental implant systems from dental imaging: a systematic review and meta-analysis," Journal of periodontal & implant science, vol. 54, no. 1, pp. 3–3, Jan. 2024, doi: 10.5051/jpis.2300160008.

[17] W. I. Ibraheem, "Accuracy of Artificial Intelligence Models in Dental Implant Fixture Identification and Classification from Radiographs: A Systematic Review," Diagnostics, vol. 14, no. 8, pp. 806–806, Apr. 2024, doi: 10.3390/diagnostics14080806.

[18] Y. Balel, K. Sağtaş, Fatih Teke, and M. A. Kurt, "Artificial Intelligence-Based Detection and Numbering of Dental Implants on Panoramic Radiographs," Clinical Implant Dentistry and Related Research, vol. 27, no. 1, Jan. 2025, doi: 10.1111/cid.70000.

[19] V. Benakatti, R. P. Nayakar, Mallikarjun Anandhalli, and Rohit Sukhasare, "Advanced deep learning techniques for recognition of dental implants," Journal of Oral Biology and Craniofacial Research, vol. 15, no. 2, pp. 215–220, Feb. 2025, doi: 10.1016/j.jobcr.2025.01.016.

[20] R. A. Lashaki, Z. Raeisi, N. Razavi, M. Goodarzi, and H. Najafzadeh, "Optimized classification of dental implants using convolutional neural networks and pre-trained models with preprocessed data," BMC Oral Health, vol. 25, no. 1, Apr. 2025, doi: 10.1186/s12903-025-05704-0.

[21] Dental implant, "'dental Implant' Dataset," Roboflow, 2024. https://universe.roboflow.com/dental-implant-nyw2h/-dental-implant (accessed Aug. 17, 2025).

[22] Y.-J. Lin et al., "Deep Learning-Assisted Diagnostic System: Implant Brand Detection Using Improved IB-YOLOv10 in Periapical Radiographs," Diagnostics, vol. 15, no. 10, p. 1194, May. 2025, doi: 10.3390/diagnostics15101194.

[23] P. Roongruangsilp, W. Narkbuakaew, and P. Khongkhunthian, "Performance of two different artificial intelligence models in dental implant planning among four different implant planning software: a comparative study," BMC Oral Health, vol. 25, no. 1, Jul. 2025, doi: 10.1186/s12903-025-06336-0.

[24] A. Khairkar, "Dental Implant Dataset," Mendeley Data, vol. 1, Sep. 2024, doi: 10.17632/x4gr6mmwy4.1.

[25] R. Varghese and S. M., "YOLOv8: A Novel Object Detection Algorithm with Enhanced Performance and Robustness," 2024 International Conference on Advances in Data Engineering and Intelligent Computing Systems (ADICS), Chennai, India, 2024, pp. 1-6, doi: 10.1109/ADICS58448.2024.10533619.

[26] M. Yaseen, "What is YOLOv8: An In-Depth Exploration of the Internal Features of the Next-Generation Object Detector," arXiv (Cornell University), Aug. 2024, doi: 10.48550/arxiv.2408.15857.

[27] C.-Y. Wang, I-Hau. Yeh, and H.-Y. M. Liao, "YOLOv9: Learning What You Want to Learn Using Programmable Gradient Information," arXiv (Cornell University), Feb. 2024, doi: 10.48550/arxiv.2402.13616.

[28] A. Wang et al., "YOLOv10: Real-Time End-to-End Object Detection," arXiv.org, May 23, 2024, doi: 10.48550/arXiv.2405.14458.

[29] [29] J. S. Jadhav, S. Yadav, K. D. Bamane, C. Chauhan, S. S. Panchikattil, A. Sengar, and P. Laxkar, "An Adaptive Hybrid Feature Fusion Framework for Interpretable Brain Tumor Classification in MRI," International Journal of Computer Information Systems and Industrial Management Applications, vol. 18, no. 6s, pp. 324–341, Jul. 2026, doi: 10.70917/ijcisim-2026-2914.

[30] P. Jain, N. Jain, S. Panchikattil, D. Chikhale, J. S. Jadhav, and A. Sankpal, "A Unified and Interpretable Benchmarking Framework for Brain Tumor Classification Using Classical and Deep Learning Models," International Journal of Drug Delivery Technology, vol. 16, no. 8s, pp. 1–6, 2026, doi: 10.25258/ijddt.16.8s.1.

[31] J. S. Jadhav, T. Shinde, D. Varma, V. Pandhare, A. Deshmukh, and V. Ladkat, "Automated Detection of Disc Degeneration in X-Ray Images Using Deep Learning CNNs," in Artificial Intelligence and Sustainable Innovation, pp. 347–351, Nov. 2025, doi: 10.1201/9781003654049-50.

[32] J. S. Jadhav and J. Deshmukh, "XAI-DiseaseDetect: Explainable and Blockchain-Enabled Early Viral Disease Detection," International Journal of Drug Delivery Technology, vol. 16, no. 21s, pp. 639–657, Apr. 2026, doi: 10.25258/ijddt.16.21s.67.